# Journal of Materials Chemistry A

Accepted Manuscript


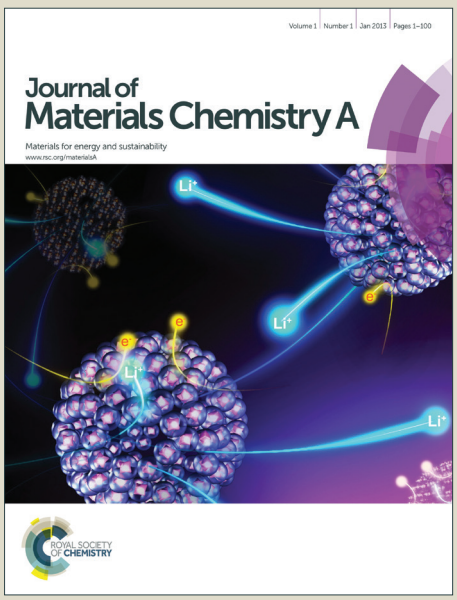





ROYAL SOCIETY OF CHEMISTRY

www.rsc.org/materialsA

# Constructing stereocomplex structure at the interface for remarkably accelerating matrix crystallization and enhancing mechanical properties of poly(L-lactide)/multi-walled carbon nanotubes nanocomposites

Huili Liu, Dongyu Bai, Hongwei Bai*, Qin Zhang, Qiang Fu*

**Abstract:** In recent years, there has been growing interest in developing poly(L-lactide)/carbon nanotubes (PLLA/CNTs) nanocomposites due to their considerable application value and potential. Unfortunately, the fabrication of high-performance PLLA/CNTs nanocomposites still faces several obstacles mainly related to low crystallization rate of PLLA matrix as well as poor interfacial adhesion between the matrix and CNTs. In this work, we demonstrate a facile and promising route to simultaneously address these limitations by compositing PLLA with poly(D-lactide) grafted multi-walled carbon nanotubes (MWCNTs-*g*-PDLA) which can be synthesized via in-situ ring-opening polymerization of D-lactide on the MWCNTs surface. During melt-mixing of PLLA with the as-prepared MWCNTs-*g*-PDLA, the grafted PDLA chains and PLLA matrix chains tend to arrange side by side at the composite interface and finally co-crystallize into stereocomplex (SC) crystallites capable of serving as not only a highly active nucleating agent to dramatically accelerate matrix crystallization but also an effective

* Corresponding author. Tel./Fax: +86 28 8546 1795. E-mail: bhw_168@163.com (H.W. Bai); qiangfu@scu.edu.cn (Q. Fu).

interfacial enhancer to greatly improve interfacial stress transfer efficiency. As a result, PLLA/MWCNTs-*g*-PDLA nanocomposites exhibit much higher matrix crystallization rate and mechanical strength as compared to PLLA/MWCNTs-*g*-PLLA counterparts where only limited physical entanglement between grafted and matrix chains forms across the interface. Moreover, both the crystallization rate and mechanical strength can be readily manipulated by tailoring the length of the grafted PDLA chains. This work could provide an access to design advanced PLLA-based nanocomposites with fast matrix crystallization ability and outstanding mechanical properties via constructing multifunctional SC crystal structure at the interface.

**Keywords:** poly(L-lactide), carbon nanotubes, stereocomplex, interface, mechanical properties

## 1. Introduction

Biodegradable polymers derived from biorenewable resources have received considerable attention over the past two decades as an answer to the growing sustainability and environmental issues associated with traditional non-biodegradable polymers derived from petroleum[1, 2]. Nowadays, poly(L-lactide) (PLLA) represents the most promising bio-derived and biodegradable polymer with tremendous application potential and has been experiencing explosive market growth in packaging and biomedical fields owing to its abundant natural raw materials (e.g., corn), competitive price, favorable biocompatibility, excellent transparency, easy melt-processability, and better mechanical performance compared to other biopolymers[3-5]. Unfortunately, even if PLLA is a crystallizable polymer with

relatively high mechanical strength, the strength is still insufficient for its applications as high-performance structural materials including aerospace or automotive parts and artificial cortical bone[6-8]; on the other hand, only amorphous articles with poor heat-resistance (heat distortion temperature is close to the low glass transition temperature, $T_g$ of ca. 50-60 ℃, much lower than highly crystallized ones where crystalline phase could confer a high resistance to deformation above $T_g$) can be obtained using traditional melt-processing technologies such as injection molding because of its very low crystallization rate[9-16], which makes PLLA unable to be used in many environments where good heat-resistance is required to avoid deformation during its service life at elevated temperatures. Therefore, it is of great interest to simultaneously enhance mechanical strength and crystallization rate of PLLA so as to substantially meet the requirements of numerous application environments.

Compositing polymers with various inorganic nanofillers provides a simple but robust way to develop high-performance polymer nanocomposites with remarkably improved mechanical strength and some added functionalities, such as impressive electrical conductivity, UV-resistance, antimicrobial activity, osteoinductivity, and gas barrier property[17-37]. Among these nanofillers, the enthusiasm for carbon nanotubes (CNTs) as advanced reinforcing fillers has largely increased since the first report in 1994 due to their unique structure as well as extraordinary mechanical, electrical, and thermal performances[17-25]. More importantly, the high aspect ratio (typically ca. 300-1000) of CNTs could allow them to provide polymers with significantly enhanced performances at relatively low loadings, in some cases less than 0.5 wt%[17,

[18, 24]. Nevertheless, achieving such efficient translation of the superior performances of CNTs into nanocomposites requires not only good dispersion of CNTs within the polymer matrix but also strong interfacial adhesion between them[17, 18, 20, 22-25, 38-40], which makes the fabrication of PLLA/CNTs nanocomposites with considerable application value become a big challenge. Even in the case of good dispersion, reinforcing efficiency of CNTs on PLLA matrix is far from theoretical expectation because the interface dominated by their poor interfacial compatibility is too weak to be able to transfer load from the PLLA matrix to the CNTs as efficiently as the bulk material[41-46]. Thus, great efforts have been devoted in recent years to enhancing CNTs dispersion and interfacial adhesion of the nanocomposites for fully reaching their performance potential[42-56]. Grafting PLLA chains onto the CNTs surface via "grafting to" or "grafting from" method is a versatile and feasible strategy to enhance the interfacial interaction through interdiffusion and physical entanglement with matrix PLLA chains across the interface[43-46]. However, only limited PLLA chains can be covalently attached on the CNTs surface because the small amounts of reactive groups available as well as the steric crowding on the surface bring negative effects on the growing of the PLLA chains. As a result, the low-density chain entanglement obtained at the interface is not sufficient enough to guarantee the efficient load transfer, thus giving rise to a limited improvement in reinforcing efficiency[43-46]. Therefore, achieving stronger interfacial adhesion via strengthening intermolecular interaction between the grafted and matrix chains is essential to realize full reinforcing potential of CNTs. On the other hand, PLLA-grafted CNTs (CNTs-*g*-PLLA) seem to have an

ability to nucleate crystallization of PLLA matrix, but they cannot serve as highly active nucleating agent (NA) because of their much lower nucleating efficiency relative to commercially available NAs and thus melt-processed articles of PLLA/CNTs-*g*-PLLA nanocomposites usually share the same amorphous matrix and resulting inferior heat-resistance with those of PLLA/CNTs nanocomposites[11, 46, 57].

With these challenges in mind, we attempted to devise a facile and promising strategy for simultaneously improving interfacial adhesion and matrix crystallization rate of PLLA/CNTs nanocomposites. Interestingly, PLLA has been reported to readily collaborate with its enantiomeric poly(D-lactide) (PDLA) and co-crystallize into stereocomplex (SC) crystallites that possess superior mechanical strength and much higher (about 50 ℃) melting temperature relative to PLLA homo-crystallites owing to the involvement of $CH_3$ ··O=C hydrogen-bonding interaction between the PLLA and PDLA chains[58-63]. More interestingly, the higher melting temperature makes it possible for SC crystallites to be reserved in PLLA melt and to act as highly active nucleating agent for homo-crystallization of PLLA or PDLA[64-70]. Inspired by these fascinating results, PDLA-grafted multi-walled CNTs (MWCNTs-*g*-PDLA) were employed as potentially advanced fillers for PLLA composites in the present work. It was expected that grafted PDLA chains on MWCNTs surface could interact with PLLA matrix chains and arrange alternatingly in a side-by-side manner under the drive of the strong shear stress involved in the melt-mixing process of PLLA and MWCNTs-*g*-PDLA, finally co-crystallizing into SC crystallites capable of acting as both interfacial enhancer and highly active NA at the interface (Scheme 1b).

Compared with the low-density chain entanglement across the interface (Scheme 1a) of traditional PLLA/MWCNTs-g-PLLA nanocomposites, the interface-localized SC crystallites involving covalently grafted PDLA chains on the MWCNTs surface and the PLLA matrix chains could endow the interface of PLLA/MWCNTs-g-PDLA nanocomposites with a much higher interfacial adhesion. Both the superior reinforcing efficiency and the nucleating efficiency of MWCNTs-g-PDLA on PLLA matrix have been demonstrated by side-by-side comparisons with MWCNTs-g-PLLA in terms of their effects on mechanical properties and matrix crystallization behaviors. More importantly, the role of the length of the grafted PDLA chains in tuning the mechanical properties and matrix crystallization rate of the PLLA/MWCNTs-g-PDLA nanocomposites is also highlighted.

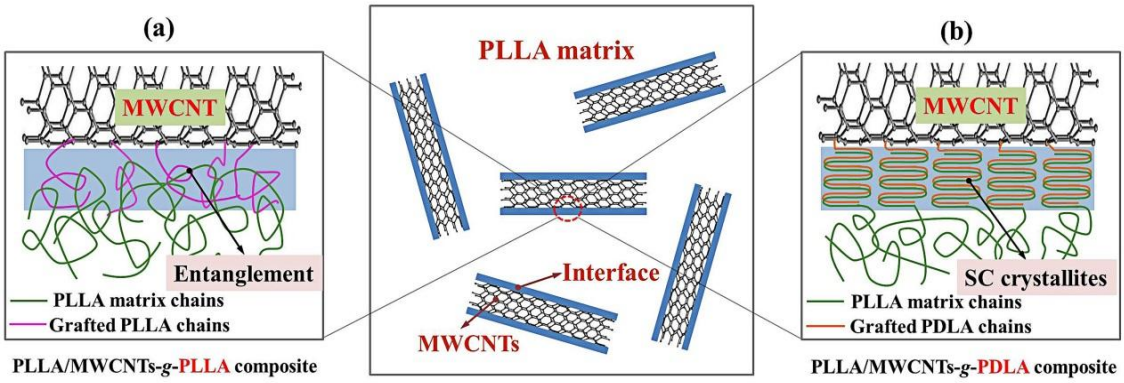


**Scheme 1.** Schematic illustration showing the interfacial microstructures of (a) PLLA/MWCNTs-*g*-PLLA and (b) PLLA/MWCNTs-*g*-PDLA nanocomposites.

## 2. Experimental section

### 2.1 Materials

Commercially available poly(L-lactide) (PLLA) containing 1.2-1.6% D-isomer was

purchased from NatureWorks LLC, U.S.A. The weight-averaged molecular weight ( $M_w$ ) and polydispersity index are 141000 g/mol and 1.74, respectively. Hydroxyl-functionalized multi-walled carbon nanotubes (MWCNTs-OH) with hydroxyl group content of approximately 3.06 wt%, diameters of 10-20 nm, and lengths of 10-30 μm were supplied by Chengdu Organic Chemicals Co. Ltd, Chinese Academy of Sciences. X-Ray photoelectron spectroscopy (XPS) spectra and Boehm titration experiment (not shown here) demonstrates that a trace amount (~0.6 wt%) of carboxyl group also exist on the MWCNTs-OH surface. L-lactide and D-lactide (purity>98.5) were obtained from Changchun SinoBiomaterials Co. Ltd., China. Tin(II)2-ethylhexanoate ($Sn(Oct)_2$) was provided by Sigma-Aldrich. Toluene, chloroform, methanol, and acetic anhydride were obtained from Chengdu Kelong Chemical Reagent Factory, China. Prior to use, both toluene and chloroform were dried over calcium hydride, and the lactide monomers were purified via recrystallization from the dry toluene. Methanol and acetic anhydride was used as received without further purification.

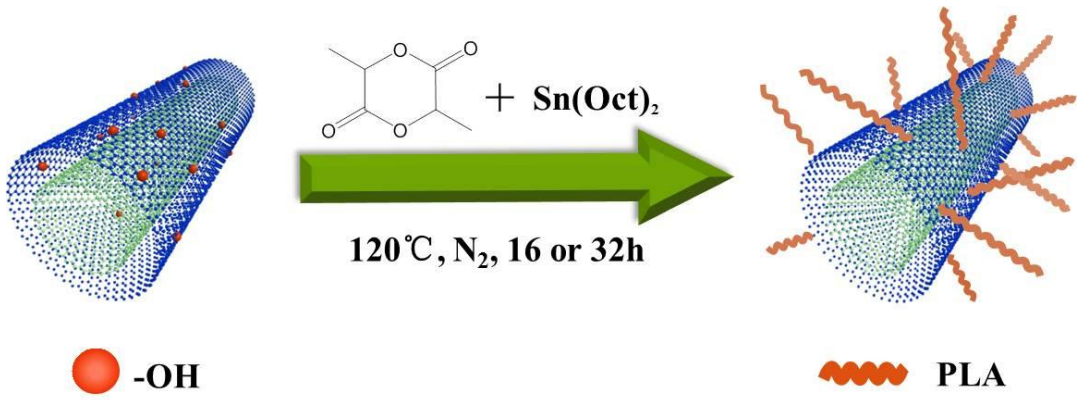


**Scheme 2.** Schematic illustration showing the synthesis of MWCNTs-*g*-PLAs via in-situ ring-opening polymerization of D-lactide or L-lactide on MWCNTs surface.

### 2.2 Synthesis of MWCNTs-*g*-PDLA and MWCNTs-*g*-PLLA nanohybrids

The synthesis of PDLA-grafted MWCNTs (MWCNTs-*g*-PDLA) nanohybrid was carried out via ring-opening polymerization of D-lactide initiated from hydroxyl groups available on the MWCNTs-OH surface using $Sn(Oct)_2$ as catalyst, as illustrated in Scheme 2. The preparation procedure can be briefly described as follows: pristine MWCNTs-OH powders were first dispersed into dry toluene under bath-type sonication at 100 W for 40 min and then transferred into a dried three-necked flask (equipped with a magnetic stirrer, a thermometer, and a nitrogen inlet) together with required amounts of purified D-lactide previously dissolved in hot dry toluene; after stirring and sonicating for 20 min under dry nitrogen atmosphere, desired amount (1.0 wt% with respect to the added D-lactide) of $Sn(Oct)_2$ was dropped into the mixture under constant stirring using a flame-dried micro syringe, followed by immersing the flask in an oil bath at 120 ℃ to allow the ring-opening polymerization to proceed under dry nitrogen atmosphere with vigorous stirring. The polymerization reaction was stopped by cooling down the flask to room temperature. The as-synthesized MWCNTs-*g*-PDLA nanohybrid was separated from the reacted products by filtering through a 0.22 μm Millipore polytetrafluoroethylene membrane, washing with excessive chloroform, and centrifugation at 8000 rpm. The filtering, washing and centrifugation processes were repeated for at least six times to completely remove the unreacted D-lactide monomer, MWCNTs-OH, and the free PDLA that did not covalently graft onto the MWCNTs surface. The final product was dried in a vacuum

oven at 60 ℃ for 24 h to remove any residual solvent. The molecular weight of the grafted PDLA chains was controlled by varying the polymerization reaction time. The obtained MWCNTs-*g*-PDLA nanohybrids are denoted as MWCNTs-*g*-PDLA1 and MWCNTs-*g*-PDLA2, respectively, according to the reaction time of 16 and 32 h. For comparison, MWCNTs-*g*-PLLA nanohybrids with two different PLLA molecular weights, denoted as MWCNTs-*g*-PLLA1 and MWCNTs-*g*-PLLA2, were also synthesized via in-situ ring-opening polymerization of L-lactide monomer on the MWCNTs-OH surface following the same procedures. The collected nanohybrids were stored in a desiccator before characterization.

### 2.3 Preparation of PLLA/MWCNTs-*g*-PDLA and PLLA/MWCNTs-*g*-PLLA nanocomposites

To achieve precise loading as well as good dispersion of MWCNTs-*g*-PDLA and MWCNTs-*g*-PLLA nanohybrids in PLLA matrix, PLLA/MWCNTs-*g*-PDLA and PLLA/MWCNTs-*g*-PLLA nanocomposites containing various amounts of MWCNTs were prepared by melt-mixing neat PLLA with corresponding PLLA/nanohybrid (95/5, wt/wt) master batch using a Haaker MiniLab II twin-screw micro-compounder (Thermo Fisher Scientific Inc., U.S.A.) at 50 rpm. The melt-mixing temperature was selected as 180 ℃ to facilitate the collaboration of PDLA chains grafted on the surface of MWCNTs-*g*-PDLA nanohybrid with surrounding PLLA matrix chains and the subsequent stereocomplex crystallization at the composite interface under the drive of strong shear stress involved in the melt-processing[71]. Specially, in order to prevent thermal degradation of the grafted PDLA and PLLA chains during the

melt-mixing process, hydroxyl end groups of the grafted chains were capped with acetic anhydride before use according to the procedure reported in the literature[72]. The PLLA/MWCNTs-*g*-PDLA and PLLA/MWCNTs-*g*-PLLA master batches were obtained by co-precipitating the homogeneous mixture of 95 wt% PLLA and 5 wt% MWCNTs-*g*-PDLA or MWCNTs-*g*-PLLA nanohybrid in chloroform solution using cold methanol as precipitator. Neat PLLA was also prepared as a control sample following the same method. Dumbbell-shaped specimens were processed by compression molding at 180 ℃ and subsequently quenching in ice water. The obtained PLLA/MWCNTs-*g*-PDLA and PLLA/MWCNTs-*g*-PLLA nanocomposites containing various amounts (0.1 to 1.5 wt%) of MWCNTs were labeled as PLLA/*x*MWCNTs-*g*-PDLA and PLLA/*x*MWCNTs-*g*-PLLA, respectively. For the purpose of morphological comparison, PLLA/MWCNTs nanocomposites denoted as PLLA/*x*MWCNTs were also prepared using the same method.

Prior to use, all materials including the as-prepared master batches were dried overnight under vacuum at 60 ℃.

**2.4 Characterizations**

2.4.1 Fourier Transform Infrared (FTIR)

FTIR spectra were recorded using a Nicolet 6700 FTIR spectrometer (Thermo Fisher Scientific Inc., U.S.A.) from 400 to 4000 $cm^{-1}$ with a resolution of 4 $cm^{-1}$ and an accumulation of 32 scans. Before the measurements, vacuum dried pristine MWCNTs-OH, MWCNTs-*g*-PDLA nanohybrid, and MWCNTs-*g*-PLLA nanohybrid were separately mixed with KBr powders and pressed into thin disk specimens.

2.4.2 Thermogravimetric Analysis (TGA)

TGA was performed using a TA Instruments Q500 analyzer (U.S.A.) in dry nitrogen atmosphere from room temperature to 500 ℃ at a heating rate of 10 ℃/min. The amount of grafted PDLA and PLLA chains on the MWCNTs surface can be evaluated by the weight loss resulting from thermal degradation of PDLA and PLLA during the heating process.

2.4.3 $^{1}$H nuclear magnetic resonance ($^{1}$H NMR)

$^{1}$H NMR spectra were recorded using a Varian Unity INOVA400 (U.S.A.) spectrometer operating at a frequency of 400 MHz. Deuterated chloroform ($CDCl_3$) and tetramethylsilane (TMS) were used as solvent and internal reference, respectively.

2.4.4 Wide-angle X-ray diffraction (WAXD)

Crystal structure was analyzed by WAXD. It was carried out on a PANalytical X'Pert pro MPD diffractometer (Holland) equipped with a CuKα radiation (λ=0.154 nm) in the diffraction angle (2θ) range of 5-30$^{o}$ at 40 kV and 40 mA.

2.4.5 Differential scanning calorimetry (DSC)

Isothermal melt crystallization kinetics was characterized using a Perkin-Elmer pyris-1 DSC (U.S.A.) under dry nitrogen atmosphere. Isothermal conditions were realized with the following DSC procedure: specimens with a weight of about 5 mg were quenched (100 ℃/min) to a desired crystallization temperature (128 ℃-138 ℃) after melting at 200 ℃ for 3 min to erase any thermal history and then held at this temperature to monitor the crystallization process until crystallization is completed. The crystallization kinetics was analyzed by the well-known Avrami equation:

$$1 - X_t = \exp(-Kt^n) \quad (1)$$

where $X_t$ is the relative crystallization fraction at time $t$, $n$ is the "Avrami exponent" depending on the type of nucleation and the growth mechanism, and $K$ is a unique rate constant associated with the nucleation and growth rate parameters. From equation (1), the half-crystallization time ($t_{0.5}$) was calculated by

$$t_{0.5} = \left(\frac{\ln 2}{k}\right)^{1/n} \quad (2)$$

Melting behavior of SC crystallites formed in the melt-quenched PLLA/MWCNTs-*g*-PDLA nanocomposites was also characterized by first DSC heating runs at a rate of 10 ℃/min from 50 to 250 ℃.

2.4.6 Polarized optical microscopy (POM)

Crystal morphology was observed using a Leica DMLP polarized optical microscopy (Germany) equipped with a Cannon digital camera (Japan). Linkam THMS600 heating and freezing stage (U.K.) was used to control the specimen temperature with an accuracy of 0.1 ℃. Specimens with a thickness of about 30 μm were prepared by hot pressing the samples sandwiched between two cover glasses at 200 ℃. After erasing thermal history at 200 ℃, specimens were rapidly cooled to a temperature of 130 ℃ at a rate of 100 ℃/min and POM observations were performed during isothermal crystallization at this temperature.

2.4.7 Scanning electron microscope (SEM)

Dispersion of MWCNTs in PLLA matrix after surface grafting PDLA or PLLA chains and fracture mechanism of PLLA/MWCNTs nanocomposites were investigated using an FEI Inspect F field emission SEM (FE-SEM, U.S.A.) at an

accelerating voltage of 5 kV. Specimens for SEM observations were obtained by cryo-fracturing the samples in liquid nitrogen. The cryo-fractured surface and tensile-fractured surface were sputter-coated with a thin layer of gold prior to imaging.

2.4.8 Transmission electron microscopy (TEM)

FEI Tecnai G2 F30 high-resolution TEM (HR-TEM, U.S.A.) operated at 200 kV was used to observe the interfacial microstructure of PLLA/MWCNTs nanocomposites before and after surface grafting modification of MWCNTs. The TEM specimens were prepared by cutting the melt-mixed nanocomposites under cryogenic conditions into thin slices using a Leica ultramicrotome (Germany) and then washing the as-prepared slices with excessive chloroform to completely remove the PLLA matrix chains that did not collaborate and co-crystallize with PDLA chains grafted on MWCNTs surface. Before observations, the obtained hybrid specimens were separately dispersed into chloroform under bath-type sonication to form a homogeneous suspension and then dripped onto a TEM grid with a layer of carbon film.

2.4.9 Tensile testing

Tensile properties were measured using an Instron 5567 universal testing machine (U.K.) at room temperature and at a cross-head speed of 2.0 mm/min. The effective dimension of dumbbell-shape specimens is 20 mm × 4 mm × 0.5 mm (length × width × thickness). For each sample, the reported value was calculated as an average of six independent specimens.

2.4.10 Dynamic rheological analysis

The melt rheology was analyzed using a HAKKE MARS rheometer with two parallel plates (25 mm in diameter). The analysis was conducted at 180 ℃ in dynamic frequency sweep mode in the range of 0.01-100 rad/s. The strain amplitude was set as 1%. The disk-shaped specimens (25 mm in diameter and 1.5 mm in thickness) were prepared by compression molding at 180 ℃.

2.4.11 Electrical conductivity measurement

Electrical conductivity was measured using a Keithley 6487 picoammeter under a constant voltage of 1 V. Before the measurement, both ends of the rectangle specimens (20 mm × 4 mm × 0.5 mm, length × width × thickness) prepared by compression molding at 180 ℃ were painted with silver paint to ensure good electrical contact between the specimens and the electrodes.

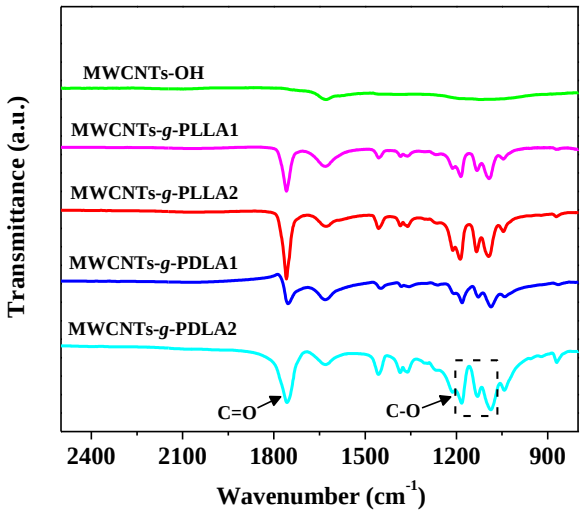


**Figure 1.** FTIR spectra of pristine MWCNTs-OH, MWCNTs-*g*-PDLA, and MWCNTs-*g*-PLLA in the wavenumber range of 800-2500 $cm^{-1}$.

## 3. Results and discussion

### 3.1 Characterization of MWCNTs-*g*-PDLA and MWCNTs-*g*-PLLA nanohybrids

MWCNTs-*g*-PDLA nanohybrids with different molecular weights of grafted PDLA chains as well as their counterparts (i.e., MWCNTs-*g*-PLLA nanohybrids) were synthesized by varying the reaction time in ring-opening polymerization of D-lactide and L-lactide monomers initiated from OH groups on the MWCNTs-OH surface. FTIR spectroscopy was performed as a direct evidence for the successful covalent grafting of PDLA and PLLA chains onto the MWCNTs surface. Figure 1 presents the recorded FTIR spectra of pristine MWCNTs-OH and surface-grafted MWCNTs nanohybrids after extensively washing with chloroform to completely remove the free PDLA and PLLA chains. Compared with the spectrum of pristine MWCNTs-OH, both MWCNTs-*g*-PDLA and MWCNTs-*g*-PLLA nanohybrids exhibit some characteristic absorption peaks of the grafted PDLA and PLLA chains. For instance, the intense peak ascribed to the carbonyl (C=O) stretching vibration at around 1758 $cm^{-1}$, and the strong peaks attributed to the symmetric C-O stretching vibrations of ester group at around 1182, 1130, and 1087 $cm^{-1}$[73, 74]. Moreover, the intensity of these characteristic peaks enhances substantially with increasing polymerization reaction time from 16 to 32 h, suggesting a greatly increased amount of the grafted chains on the MWCNTs surface. This suggestion is well supported by the TGA data displayed in Figure 2. Noticeably, MWCNTs-*g*-PDLA1 and MWCNTs-*g*-PLLA1 nanohybrids synthesized with a reaction time of 16 h show the same major weight loss (about 34 %) in the temperature range of 250-350 ℃ due to the thermal decomposition of the

grafted PDLA and PLLA chains whereas the pristine MWCNTs-OH reveals no appreciable weight loss during the heating process up to 450 ℃, which allows us to directly estimate the amount of the grafted chains in the nanohybrids using the weight loss recorded at 450 ℃. The grafted amount rises to as high as 80.5 wt% in MWCNTs-*g*-PDLA2 nanohybrid and 74.5 wt% in MWCNTs-*g*-PLLA2 nanohybrid with further increasing the reaction time to 32 h (Table 1), signifying that much longer PDLA and PLLA chains have been chemically grafted onto the MWCNTs surface. The ratios of recovered MWCNTs-g-PDLA and MWCNTs-g-PLLA nanohybrids relative to MWCNTs-OH in the feed also suggests similar grafted amounts (Table 1).

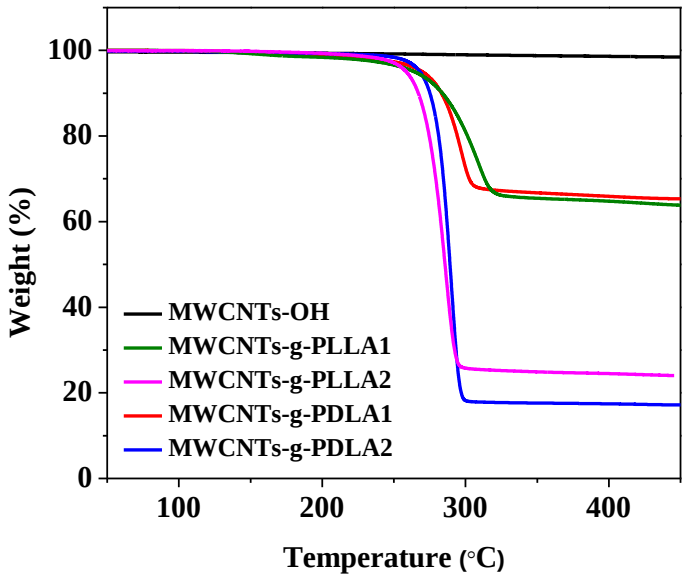


**Figure 2.** TGA curves of pristine MWCNTs-OH, MWCNTs-*g*-PDLA, and MWCNTs-*g*-PLLA.

High-resolution $^{1}$H NMR spectroscopy was utilized to determine the absolute molecular weight of the grafted PDLA and PLLA chains on the MWCNTs surface,

and the $^{1}$H NMR spectra of the MWCNTs-*g*-PLLA and MWCNTs-*g*-PDLA nanohybrids are shown in Figure 3. The peak "**A**" at around 5.16 ppm and the peak "**a**" at around 4.35 ppm are attributed to the methine protons connected with the ester groups within the chain backbone and the hydroxyl groups at the chain end, respectively. The number-average molecular weight ($M_n$) of the grafted chains was approximately calculated according to the following equation[75]:

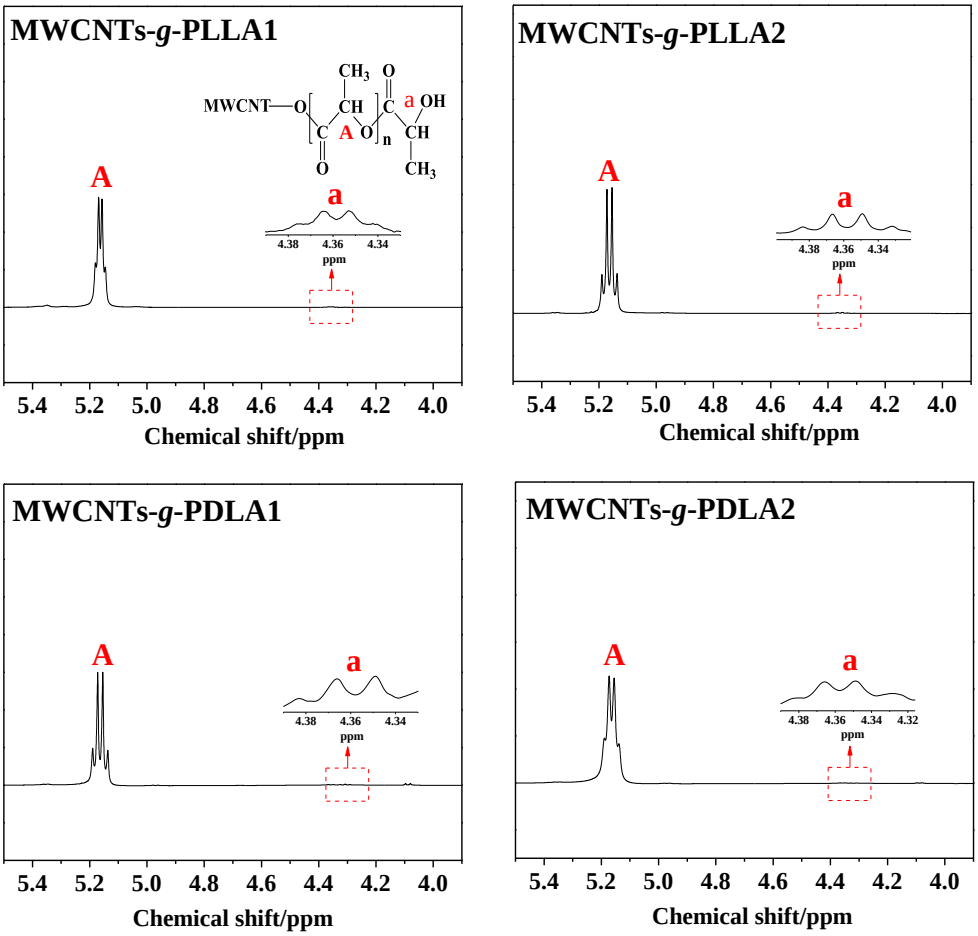


**Figure 3.** $^{1}$H NMR spectra of MWCNTs-*g*-PLLA and MWCNTs-*g*-PDLA. The calculated number-average molecular weights of the grafted PLLA and PDLA chains on MWCNTs surface are given in the profiles.

$$M_n = \left[ \left( \frac{A_A}{A_a} \right) + 1 \right] \times 72 + 57 \qquad (3)$$

where $A_A$ and $A_a$ represent the integrated intensity of the two peaks "**A**" and "**a**", respectively. As expected, the $M_n$ increases evidently with the increase of the reaction time, and the MWCNTs-*g*-PLLA2 and MWCNTs-*g*-PDLA2 nanohybrids share a similar $M_n$ of about 25500-27500 g/mol (Table 1), which is more than twice as high as the MWCNTs-*g*-PLLA1 and MWCNTs-*g*-PDLA1 nanohybrids.

**Table 1.** The parameters of the as-synthesized MWCNTs-g-PDLA and MWCNTs-g-PLLA nanohybrids.

| Samples | Amount of the grafted PLLA or PDLA chains (wt%)[a] | $M_n$ (g/mol)[b] | Ratios of recovered nanohybrids relative to MWCNTs-OH in the feed |
|---|---|---|---|
| MWCNTs-g-PLLA1 | 34.8 | 10680 | 0.58/0.40 |
| MWCNTs-g-PLLA2 | 74.5 | 25606 | 1.47/0.40 |
| MWCNTs-g-PDLA1 | 34.0 | 10103 | 0.56/0.40 |
| MWCNTs-g-PDLA2 | 80.5 | 27369 | 1.86/0.40 |

[a] obtained from TGA curves, [b] evaluated by $^1$H NMR spectra.

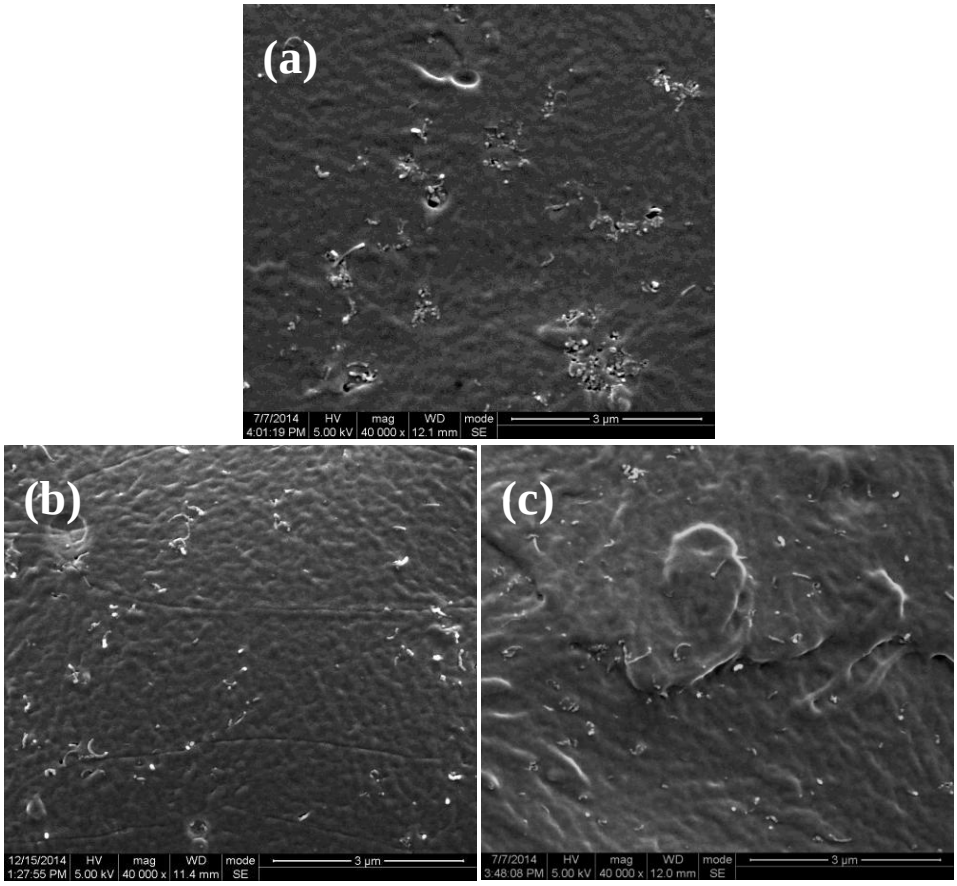


**Figure 4.** SEM images of cryo-fractured surfaces of (a) PLLA/1MWCNTs-OH, (b) PLLA/1MWCNTs-*g*-PLLA2, and (c) PLLA/1MWCNTs-*g*-PDLA2 nanocomposites.

### 3.2 Morphology and interfacial microstructure of PLLA nanocomposites

PLLA/MWCNTs-*g*-PDLA and PLLA/MWCNTs-*g*-PLLA nanocomposites were prepared by separately introducing the synthesized MWCNTs-*g*-PDLA and MWCNTs-*g*-PLLA nanohybrids into PLLA matrix through melt-mixing. Different from the physical entanglement between the grafted and matrix chains across the interface of the PLLA/MWCNTs-*g*-PLLA nanocomposites, SC crystallites are expected to form at the interface of the PLLA/MWCNTs-*g*-PDLA nanocomposites

through co-crystallization between the PLLA matrix and grafted PDLA chains. The dispersion of various MWCNTs in the PLLA matrix was characterized by SEM and some representative SEM images are illustrated in Figure 4. Without grafting, MWCNTs tend to aggregate into big and compact agglomerates with diameter of about 0.5-2.5 μm, and the interface between the MWCNTs and PLLA matrix is very clear due to the poor compatibility between them (Figure 4a). However, the grafting of PLLA chains onto the surface can significantly improve the dispersion of MWCNTs as well as the interfacial interaction by sterically hindering the aggregation of the MWCNTs and enhancing the interfacial compatibility (Figure 4b). The agglomerate size becomes much smaller and the interface debonding cannot be easily discernible. More interestingly, almost the same good MWCNTs dispersion and interface compatibility are noticed for PLLA/MWCNTs-*g*-PDLA nanocomposites (Figure 4c). Most of the MWCNTs-*g*-PDLA nanohybrids are uniformly dispersed in the matrix and interact strongly with the matrix, suggesting that SC crystallites capable of not only hindering the aggregation of the nanohybrids as barrier but also enhancing the interface interaction as linker are most likely formed at the interface.

The interfacial microstructure of these nanocomposites was analyzed by TEM as an indirect method after completely removing the free PLLA matrix chains. As shown in Figure 5a, the surface of pristine MWCNTs is quite smooth and clear due to the absence of any grafted chains on the surface, which is believed to be responsible for the clear interface displayed in Figure 4a. In contrast, the MWCNTs extracted from PLLA/MWCNTs-*g*-PLLA nanocomposites appear very coarse and stained with a thin

layer of covalently grafted PLLA phase (gray area as highlighted by the arrows in Figure 5b), implying that the significantly enhanced interfacial adhesion (Figure 4b) is associated with the formation of chain entanglement between the grafted PLLA and PLLA matrix chains across the interface. As for PLLA/MWCNTs-*g*-PDLA nanocomposites, some protuberances that are presumed to come from SC crystallites

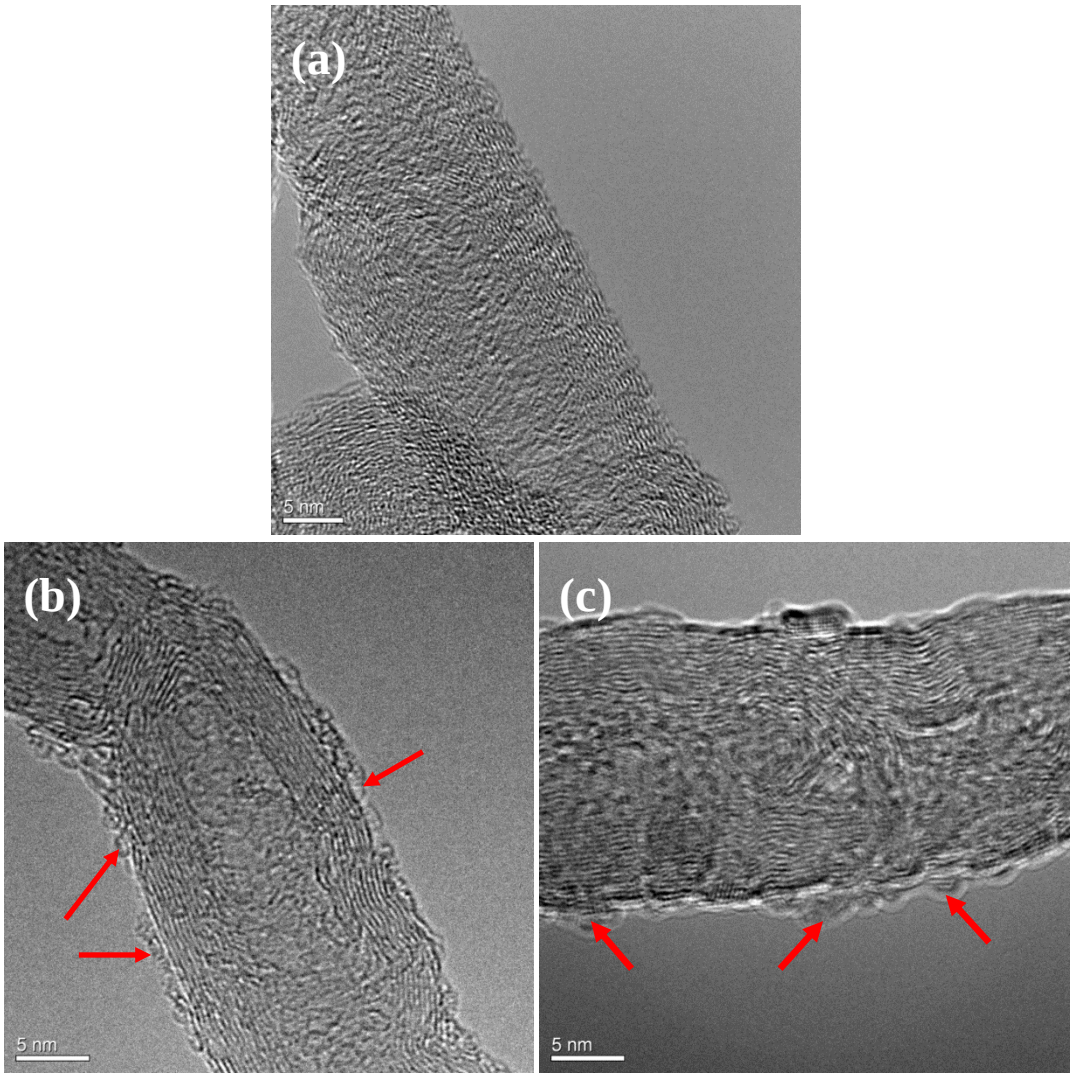


**Figure 5.** TEM images showing the microstructures at the interfaces of melt-processed (a) PLLA/1MWCNTs-OH, (b) PLLA/1MWCNTs-*g*-PLLA2, and (c) PLLA/1MWCNTs-*g*-PDLA2 nanocomposites after washing with chloroform.

can be observed on the surface of the extracted MWCNTs (Figure 5c). WAXD analysis provides a direct evidence for the formation of the SC crystallites in the PLLA/MWCNTs-*g*-PDLA nanocomposites. As presented in Figure 6d, the WAXD diffraction pattern of melt-quenched PLLA/MWCNTs-*g*-PDLA2 nanocomposites exhibits three characteristic diffraction peaks at about 12.0 °, 21.0 ° and 24.0 °, corresponding to the (110), (300)/(030), and (220) planes of SC crystal structure,[58] and the intensity of these diffraction peaks enhances obviously with increasing the amount of MWCNTs-*g*-PDLA2 nanohybrids up to 1 wt%. These results distinctly demonstrate the formation of SC crystallites at the interface during the melt-mixing of PLLA matrix and the MWCNTs-*g*-PDLA nanohybrids. Please note that, because the amount of the grafted PDLA chains in MWCNTs-*g*-PDLA1 nanohybrids is much lower than that in the MWCNTs-*g*-PDLA2 ones (Figure 2) and then only trace amounts of SC crystallites could be formed in PLLA/MWCNTs-*g*-PDLA1 nanocomposites, no obvious characteristic peaks of SC structure are noticed in the diffraction patterns (Figure 6c). With regard to melt-quenched PLLA/MWCNTs-g-PLLA nanocomposites, the lack of the grafted PDLA chains on the MWCNTs surface makes it impossible to form SC structure at the interface (Figure 6a and b).

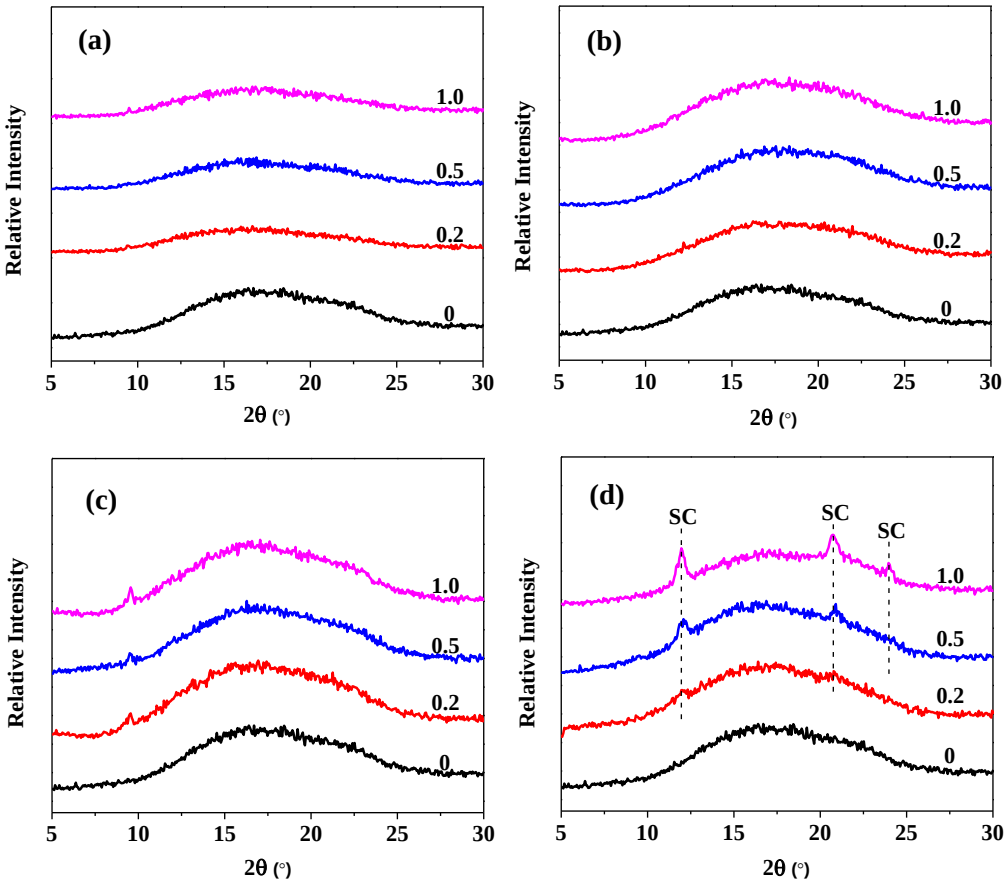


**Figure 6.** WAXD patterns of melt-quenched nanocomposites containing various amounts (wt%) of MWCNTs: (a) PLLA/MWCNTs-*g*-PLLA1, (b) PLLA/MWCNTs-*g*-PLLA2, (c) PLLA/MWCNTs-*g*-PDLA1, and (d) PLLA/MWCNTs-*g*-PDLA2.

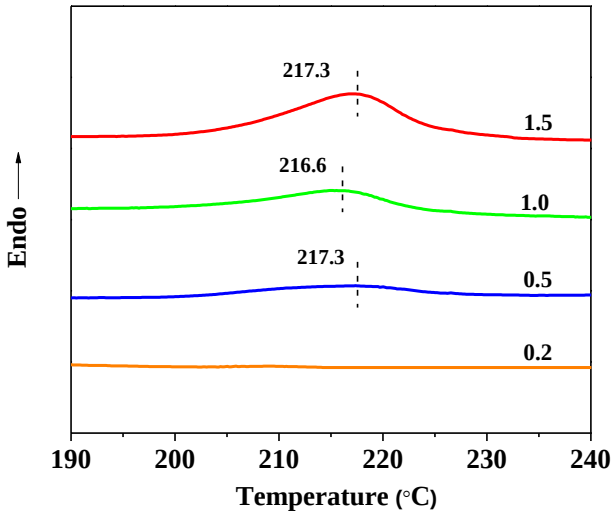


**Figure 7.** DSC heating curves of melt-quenched PLLA/MWCNTs-g-PDLA2 nanocomposites containing various amounts (wt%) of MWCNTs.

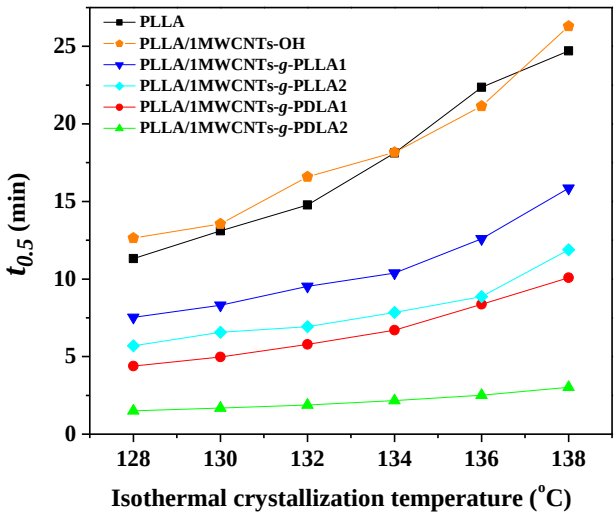


**Figure 8.** Half-crystallization time ($t_{0.5}$) as a function of isothermal crystallization temperature for neat PLLA, PLLA/MWCNTs-OH and PLLA/MWCNTs-*g*-PLAs nanocomposites containing 1.0 wt% MWCNTs.

### 3.3 Matrix crystallization behavior and mechanical properties of PLLA nanocomposites

It is well known that interfacial microstructure plays a key role in determining the performance of polymer nanocomposites[25, 40]. Compared with PLLA/MWCNTs-*g*-PLLA nanocomposites with limited chain entanglement across the interface, significantly enhanced matrix crystallization and mechanical strength could be realized in PLLA/MWCNTs-*g*-PDLA nanocomposites because the interface-localized SC crystallites are expected to serve as both highly active nucleating agent to accelerate matrix crystallization and effective interfacial enhancer to improve interfacial stress transfer efficiency. To provide a clear-cut evidence for the effectiveness of the SC crystallites as highly active nucleating agents on PLLA matrix crystallization, isothermal crystallization behaviors of PLLA/MWCNTs, PLLA/MWCNTs-*g*-PDLA, and PLLA/MWCNTs-*g*-PLLA nanocomposites were comparatively investigated using DSC and POM. Before monitoring the crystallization at various temperatures, all the samples were melted at 200 ℃ (above the melting temperature of PLLA or PDLA homo-crystallites but below the melting temperature of SC crystallites) to completely erase the thermal history of the PLLA matrix but reserve the SC crystallites in the melt. The melting temperature of the SC crystallites formed in PLLA/MWCNTs-*g*-PDLA nanocomposites is about 217 ℃ (Figure 7). Figure 8 shows the variation of half-crystallization time ($t_{0.5}$) as a function of isothermal crystallization temperature. Obviously, the values of $t_{0.5}$ (an indicator of crystallization rate[11]) of PLLA matrix are almost unchanged with the addition of

pristine MWCNTs, while the addition of MWCNTs-*g*-PLLA nanohybrids leads to an evidently enhanced matrix crystallization rate and the enhancement of the crystallization rate increases apparently with the amount of the grafted PLLA chains whose one end is pinned to MWCNTs surface, indicating that the grafted chains can act as nucleating agent to accelerate PLLA crystallization. However, it is noticeable that their nucleating efficiency is much lower than MWCNTs-*g*-PDLA nanohybrids. Even for PLLA/1MWCNTs-*g*-PDLA1 nanocomposite with only trace amounts of SC crystallites at the interface, the crystallization rate of PLLA matrix is still higher than PLLA/1MWCNTs-*g*-PLLA2 nanocomposite at the same crystallization temperatures. Specially, the value of $t_{0.5}$ obtained at 132 ℃ decreases dramatically from 16.6 min for PLLA/1MWCNTs nanocomposite to as low as 1.9 min for PLLA/1MWCNTs-*g*-PDLA2 nanocomposite, which confirms the same strong heterogeneous nucleating effect of the interface-localized SC crystallites on PLLA matrix crystallization as the highly active nucleating agent N,N',N''-tricyclohexyl-1,3,5-benzene-tricarboxylamide reported in our previous work[76]. The high nucleating efficiency of the SC crystallites on the PLLA matrix crystallization can be further demonstrated by POM observations as shown in Figure 9, with a special attention on the crystallization rate and nucleation density. It is clear that both PLLA/1MWCNTs-*g*-PLLA1 and PLLA/1MWCNTs-*g*-PLLA2 nanocomposites have a similar low nucleation density (Figure 9a and b). The spherulites grow slowly and only large spherulites with average diameter of around 30-50 μm can be obtained. In contrast, more and smaller spherulites are observed in

PLLA/1MWCNTs-*g*-PDLA1 nanocomposite with a very small amount of SC crystallites at the interface (Figure 9c and d). Especially for the PLLA/1MWCNTs-*g*-PDLA2 nanocomposite, the size of the PLLA spherulites is found to decrease dramatically and thus it is difficult to differentiate the tiny spherulites one by one. The decreased spherulite size could gives to an enhanced mechanical strength of PLLA[77].

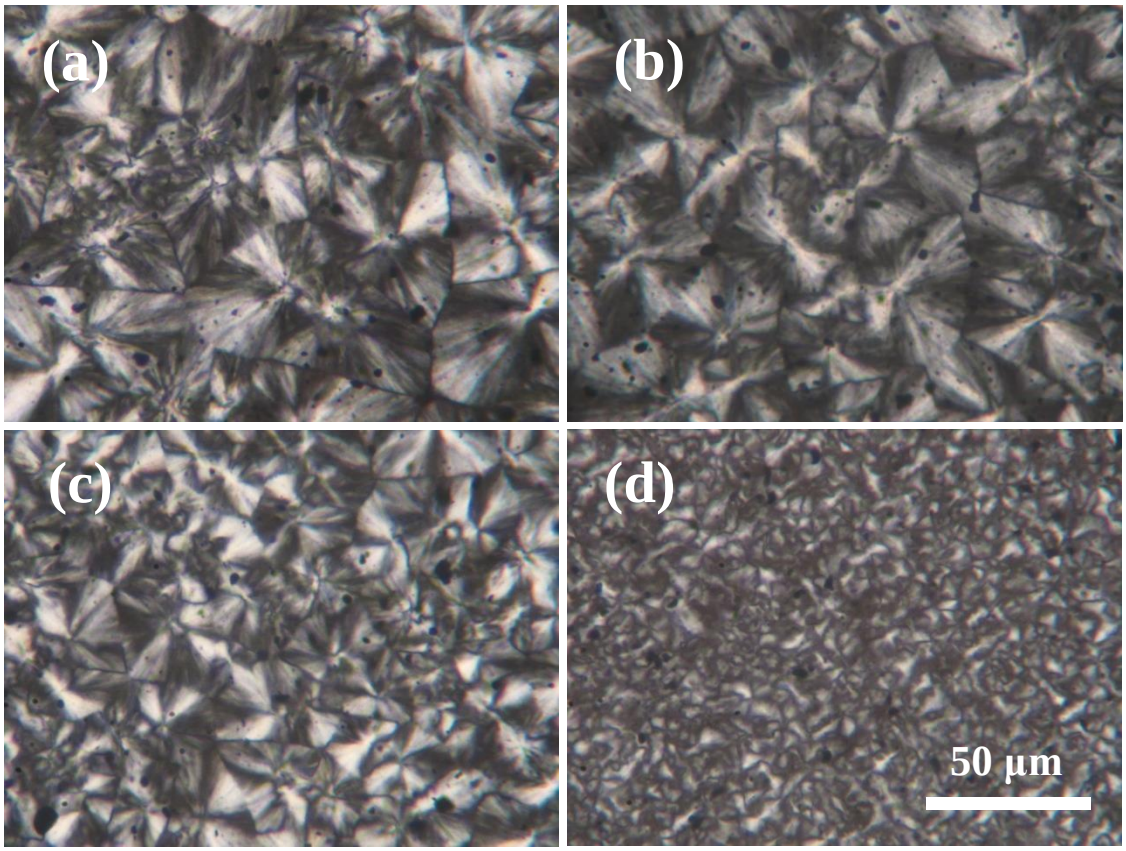


**Figure 9.** POM images showing the crystalline morphologies of (a) PLLA/1MWCNTs-*g*-PLLA1, (b) PLLA/1MWCNTs-*g*-PLLA2, (c) PLLA/1MWCNTs-*g*-PDLA1, and (d) PLLA/1MWCNTs-*g*-PDLA2 nanocomposites after completion of isothermal crystallization at 130 ℃.

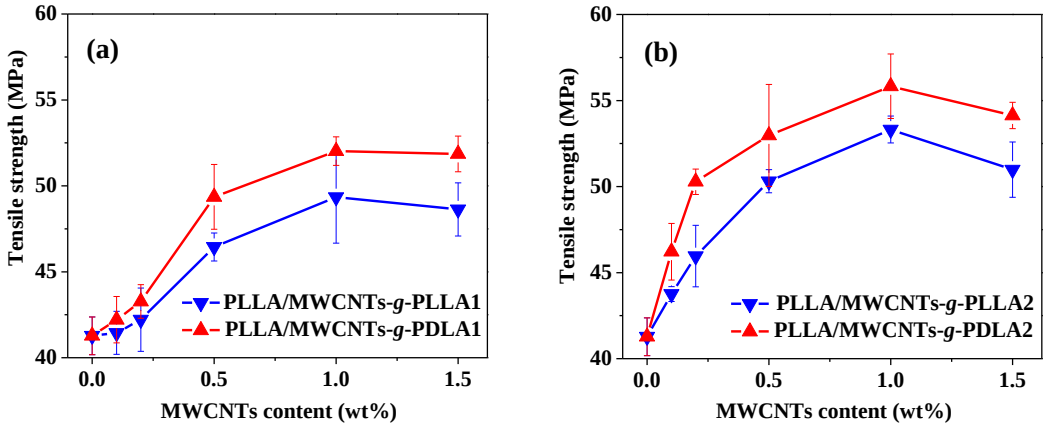


**Figure 10.** Tensile strength of PLLA/MWCNTs-*g*-PDLA and PLLA/MWCNTs-*g*-PLLA nanocomposites as a function of MWCNTs content.

To illuminate the potential of the SC crystallites tailored interfacial adhesion on the mechanical reinforcement of PLLA/MWCNTs nanocomposites, the effects of MWCNTs-*g*-PDLA and MWCNTs-*g*-PLLA nanohybrids on the mechanical properties of PLLA matrix were comparatively studied by uniaxial tensile testing. Figure 10 illustrates the obtained tensile strength as a function of MWCNTs content. Evidently, introduction of 0.5-1.5 wt% MWCNTs-*g*-PLLA nanohybrids into the PLLA matrix induces a significantly enhanced tensile strength (Figure 10a). Moreover, the obtained reinforcement efficiency is strongly dependent on the interfacial adhesion between the matrix and MWCNTs (Figure 10a and b). With the increase in the PLLA chain length or the grafted amount on the MWCNTs surface, the tensile strength of PLLA/MWCNTs-*g*-PLLA nanocomposites increases obviously probably because of the increased density of chain entanglement across the interface (Figure 10a). Similar results are also reported in PLLA/$SiO_2$-*g*-PLLA nanocomposites[75]. More interestingly,

once some SC crystallites instead of chain entanglement are formed at the interface, superior reinforcement efficiency can be easily achieved in PLLA/MWCNTs-*g*-PDLA nanocomposites at the same MWCNTs contents and grafted amounts as compared with the PLLA/MWCNTs-*g*-PLLA ones (Figure 10b), indicating that the interface-localized SC crystallites can impart stronger interfacial adhesion just as the hinge between the door and the door frame. In particular, the tensile strength of PLLA/1MWCNTs-*g*-PDLA2 nanocomposite is 55.8 MPa, in comparison with 49.4 MPa of PLLA/1MWCNTs-*g*-PLLA2 nanocomposite. In order to get a better understanding on the fracture mechanism of PLLA/MWCNTs-g-PLLA and PLLA/MWCNTs-g-PDLA nanocomposites, SEM was used to observe the tensile-fractured surfaces. As shown in Figure 11, the degree of interfacial debonding decreases apparently with the formation of SC crystallites in the nanocomposites, clearly demonstrating that the interfacial-localized SC crystallites can serve as interfacial enhancer to greatly improve interfacial stress transfer efficiency and the resulting reinforcement efficiency of MWCNTs on PLLA matrix.

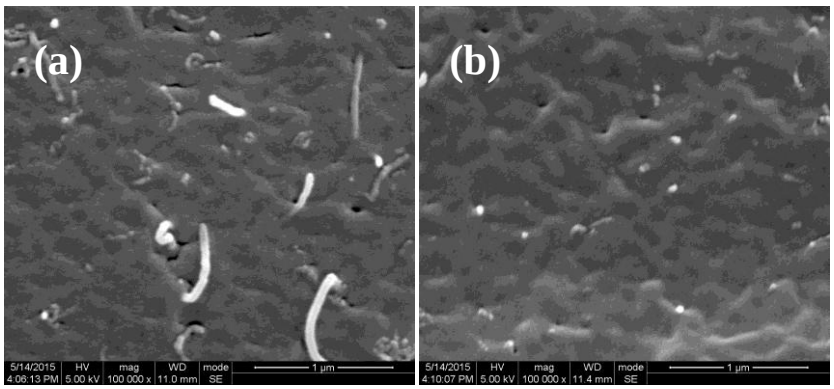


**Figure 11.** SEM images of tensile-fractured surfaces of (a) PLLA/MWCNTs-g-PLLA and (b) PLLA/MWCNTs-g-PDLA nanocomposites containing 1.0 wt% MWCNTs.

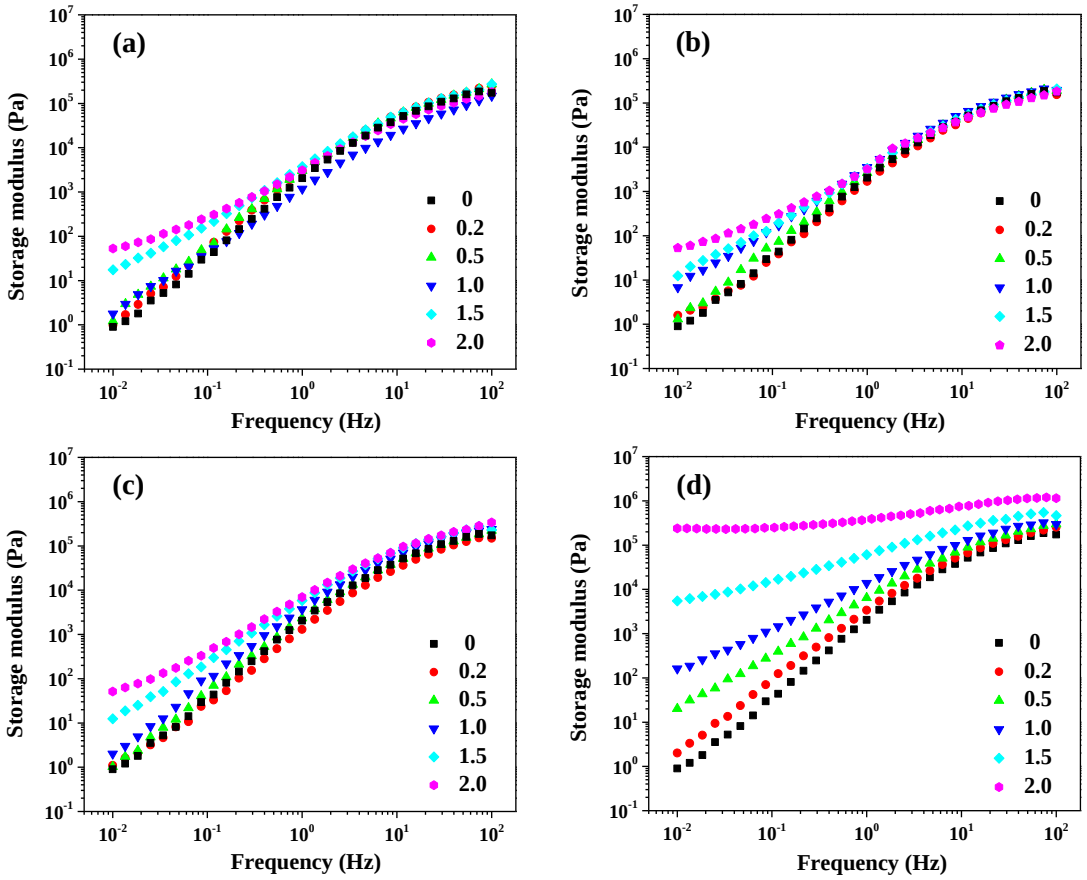


**Figure 12.** Frequency dependence of storage modulus ( $G'$ ) of (a) PLLA/MWCNTs-*g*-PLLA1, (b) PLLA/MWCNTs-*g*-PLLA2, (c) PLLA/MWCNTs-*g*-PDLA1, and (d) PLLA/MWCNTs-*g*-PDLA2 nanocomposites containing various amounts (wt%) of MWCNTs.

### 3.4 Rheological and electrical properties of PLLA nanocomposites

Melt rheology is very sensitive to the formation and evolution of percolated network structures in polymer melt, so the rheological properties of PLLA/MWCNTs-*g*-PLLA and PLLA/MWCNTs-*g*-PDLA nanocomposites were explored by an oscillatory shear rheometer at 180 ℃, where the formed SC crystallites in the PLLA/MWCNTs-*g*-PDLA nanocomposites can be reserved in the

melt. Figure 12 displays the frequency dependences of storage modulus ($G'$) for these nanocomposites. The appearance of a low-frequency plateau is an indicator of the formation of rheological percolation network. It is obvious that PLLA/MWCNTs-*g*-PLLA and PLLA/MWCNTs-*g*-PDLA1 nanocomposites exhibit almost the same rheological percolation threshold coming from MWCNTs network (Figure 12a-c). When MWCNTs content reaches to 2.0 wt %, a low-frequency plateau appears. In contrast, much higher $G'$ and lower rheological percolation threshold can be observed in the PLLA/MWCNTs-*g*-PDLA2 nanocomposites (Figure 12d) due to the formation of SC crystallite network in the melt, indicating that SC crystallites can be used as a rheological modifier to significantly improve the melt strength of the nanocomposites.

To explore the influence of the interfacial structure on the electrical percolation thresholds (i.e., the critical MWCNTs concentration needed for the formation of effective conductive network) of PLLA/MWCNTs nanocomposites, the electrical conductivity of PLLA/MWCNTs-*g*-PLLA and PLLA/MWCNTs-*g*-PDLA nanocomposites as a function of MWCNTs content are presented in Figure 13. Clearly, no apparent difference in the electrical percolation thresholds can be observed, further demonstrating that both the two nanocomposites share the same MWCNTs dispersion (Figure 4b and c).

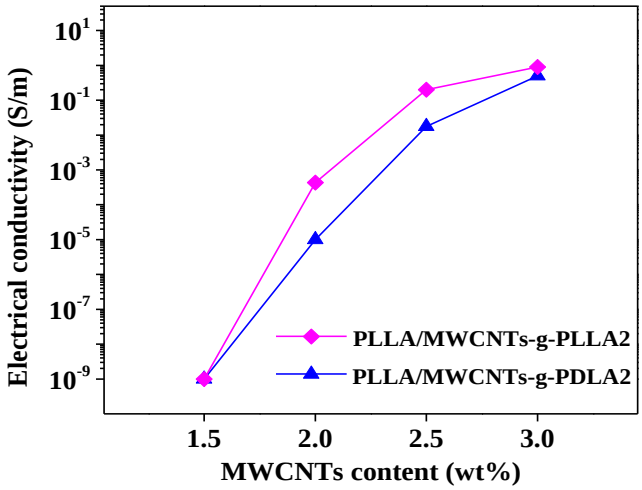


**Figure 13.** Electrical conductivity of PLLA/MWCNTs-*g*-PLLA and PLLA/MWCNTs-*g*-PDLA nanocomposites containing various amounts (wt%) of MWCNTs.

## 4. Conclusions

In conclusion, we have demonstrated that melt-mixing of PLLA with MWCNTs-g-PDLA is a facile strategy to design high-performance PLLA/MWCNTs nanocomposites with significantly enhanced mechanical strength and matrix crystallization rate. PDLA chains can be covalently grafted onto the MWCNTs-OH surface via in-situ ring-opening polymerization of D-lactide monomer, as identified by FT-IR, TGA, and $^{1}$H NMR analysis. WAXD and TEM results indicate that the grafted PDLA chains can readily interact with PLLA matrix chains during melt-processing of PLLA/MWCNTs-g-PDLA nanocomposites and finally co-crystallize into multifunctional SC crystal structure across the interface. In comparison with usually

obtained PLLA/MWCNTs-*g*-PLLA nanocomposites where the interface is dominated by limited physical entanglement between grafted and matrix chains duo to the low grafting density, the PLLA/MWCNTs-g-PDLA nanocomposites exhibit not only an evidently higher mechanical strength but also a much faster matrix crystallization at the same MWCNTs content and grafted chain length because the interface-localized SC crystallites can serve as both effective interfacial enhancer and highly active nucleating agent to simultaneously improve interfacial adhesion and matrix crystallization rate. More importantly, the critical role of increased length of the grafted PDLA chains in enhancing the reinforcing efficiency and the nucleating efficiency has been confirmed. We believe that this work could provide an avenue to fabricate advanced PLA-based nanocomposites with optimized properties.

**Acknowledgments:** This work was financially supported by National Natural Science Foundation of China (Nos. 51421061 and 21404075), China Postdoctoral Science Foundation (No. 2014T70869), State Key Laboratory of Polymer Materials Engineering (No. sklpme2015-3-01), and Scientific Research Foundation for Young Teachers of Sichuan University (No. 2015SCU11007).

**References:**

1. M. J. L. Tschan, E. Brule, P. Haquette and C. M. Thomas, *Polym. Chem.*, 2012, **3**, 836-851.
2. M. M. Reddy, S. Vivekanandhan, M. Misra, S. K. Bhatia and A. K. Mohanty, *Prog. Polym. Sci.*, 2013, **38**, 1653-1689.

3. L. T. Lim, R. Auras and M. Rubino, *Prog. Polym. Sci.*, 2008, **33**, 820-852.

4. K. M. Nampoothiri, N. R. Nair and R. P. John, *Bioresour. Technol.*, 2010, **101**, 8493-8501.

5. J. W. Rhim, H. M. Park and C. S. Ha, *Prog. Polym. Sci.*, 2013, **38**, 1629-1652.

6. Z. K. Hong, X. Y. Qiu, J. R. Sun, M. X. Deng, X. S. Chen and X. B. Jing, *Polymer*, 2004, **45**, 6699-6706.

7. R. M. Rasal, A. V. Janorkar and D. E. Hirt, *Prog. Polym. Sci.*, 2010, **35**, 338-356.

8. Q. W. Zhang, V. N. Mochalin, I. Neitzel, K. Hazeli, J. J. Niu, A. Kontsos, J. G. Zhou, P. I. Lelkes and Y. Gogotsi, *Biomaterials*, 2012, **33**, 5067-5075.

9. H. B. Li and M. A. Huneault, *Polymer*, 2007, **48**, 6855-6866.

10. A. M. Harris and E. C. Lee, *J. Appl. Polym. Sci.*, 2008, **107**, 2246-2255.

11. S. Saeidlou, M. A. Huneault, H. B. Li and C. B. Park, *Prog. Polym. Sci.*, 2012, **37**, 1657-1677.

12. H. W. Bai, C. M. Huang, H. Xiu, Q. Zhang and Q. Fu, *Polymer*, 2014, **55**, 6924-6934.

13. S. Fujisawa, J. Q. Zhang, T. Saito, T. Iwata and A. Isogai, *Polymer*, 2014, **55**, 2937-2942.

14. H. Tang, J. B. Chen, Y. Wang, J. Z. Xu, B. S. Hsiao, G. J. Zhong and Z. M. Li, *Biomacromolecules*, 2012, **13**, 3858-3867.

15. H. Xu, G. J. Zhong, Q. Fu, J. Lei, W. Jiang, B. S. Hsiao and Z. M. Li, *ACS Appl. Mater. Interfaces*, 2012, **4**, 6773-6783.

16. H. W. Bai, C. M. Huang, H. Xiu, Q. Zhang, H. Deng, K. Wang, F. Chen and Q. Fu, *Biomacromolecules*, 2014, **15**, 1507-1514.

17. M. Moniruzzaman and K. I. Winey, *Macromolecules*, 2006, **39**, 5194-5205.

18. J. B. Gao, M. E. Itkis, A. P. Yu, E. Bekyarova, B. Zhao and R. C. Haddon, *J. Am. Chem. Soc.*, 2005, **127**, 3847-3854.

19. W. Yan, Y. Zhang, H. W. Sun, S. W. Liu, Z. G. Chi, X. D. Chen and J. R. Xu, *J. Mater. Chem. A*, 2014, **2**, 20958-20965.

20. S. Roy, T. Das, Y. Ming, X. L. Chen, C. Y. Yue and X. Hu, *J. Mater. Chem. A*, 2014, **2**, 3961-3970.

21. C. M. Huang, H. W. Bai, H. Xiu, Q. Zhang and Q. Fu, *Compos. Sci. Technol.*, 2014, **102**, 20-27.

22. P. Costa, J. Silva, A. Anson-Casaos, M. T. Martinez, M. J. Abad, J. Viana and S. Lanceros-Mendez, *Compos., Part B: Eng.*, 2014, **61**, 136-146.

23. Y. Gao, G. Y. Zong, H. W. Bai and Q. Fu, *Chinese J. Polym. Sci.*, 2014, **32**, 245-254.

24. H. Z. Geng, R. Rosen, B. Zheng, H. Shimoda, L. Fleming, J. Liu and O. Zhou, *Adv. Mater.*, 2002, **14**, 1387-1390.

25. Y. D. Liu and S. Kumar, *ACS Appl. Mater. Interfaces*, 2014, **6**, 6069-6087.

26. N. Y. Ning, W. Zhang, J. J. Yan, F. Xu, T. N. Wang, H. Su, C. Y. Tang and Q. Fu, *Polymer*, 2013, **54**, 303-309.

27. M. Zhou, Y. H. Li, C. He, T. X. Jin, K. Wang and Q. Fu, *Compos. Sci. Technol.*, 2014, **91**, 22-29.

28. J. C. Fricain, S. Schlaubitz, C. Le Visage, I. Arnault, S. M. Derkaoui, R. Siadous, S. Catros, C. Lalande, R. Bareille, M. Renard, T. Fabre, S. Cornet, M. Durand, A. Leonard, N. Sahraoui, D. Letourneur and J. Amedee, *Biomaterials*, 2013, **34**, 2947-2959.

29. H. Xu, L. Xie, X. Jiang, M. Hakkarainen, J. B. Chen, G. J. Zhong and Z. M. Li, *Biomacromolecules*, 2014, **15**, 1676-1686.

30. A. J. Svagan, A. Akesson, M. Cardenas, S. Bulut, J. C. Knudsen, J. Risbo and D. Plackett, *Biomacromolecules*, 2012, **13**, 397-405.

31. M. Murariu, A. Doumbia, L. Bonnaud, A. L. Dechief, Y. Paint, M. Ferreira, C. Campagne, E. Devaux and P. Dubois, *Biomacromolecules*, 2011, **12**, 1762-1771.

32. A. L. Goffin, J. M. Raquez, E. Duquesne, G. Siqueira, Y. Habibi, A. Dufresne and P. Dubois, *Biomacromolecules*, 2011, **12**, 2456-2465.

33. F. M. Xiang, P. Tzeng, J. S. Sawyer, O. Regev and J. C. Grunlan, *ACS Appl. Mater. Interfaces*, 2014, **6**, 6040-6048.

34. S. L. Phua, L. P. Yang, C. L. Toh, G. Q. Ding, S. K. Lau, A. Dasari and X. H. Lu, *ACS Appl. Mater. Interfaces*, 2013, **5**, 1302-1309.

35. A. M. Diez-Pascual and A. L. Diez-Vicente, *ACS Appl. Mater. Interfaces*, 2014, **6**, 9822-9834.

36. M. Sabzi, L. Jiang, F. Liu, I. Ghasemi and M. Atai, *J. Mater. Chem. A*, 2013, **1**, 8253-8261.

37. P. P. Chen, Y. Wang, T. Wei, Z. Meng, X. D. Jia and K. Xi, *J. Mater. Chem. A*,

2013, **1**, 9028-9032.

38. K. S. Khare, F. Khabaz and R. Khare, *ACS Appl. Mater. Interfaces*, 2014, **6**, 6098-6110.

39. J. N. Coleman, U. Khan, W. J. Blau and Y. K. Gun'ko, *Carbon*, 2006, **44**, 1624-1652.

40. N. Y. Ning, S. R. Fu, W. Zhang, F. Chen, K. Wang, H. Deng, Q. Zhang and Q. Fu, *Prog. Polym. Sci.*, 2012, **37**, 1425-1455.

41. J. M. Raquez, Y. Habibi, M. Murariu and P. Dubois, *Prog. Polym. Sci.*, 2013, **38**, 1504-1542.

42. H. F. Wang, C. Wu, X. Liu, J. Sun, G. M. Xia, W. Huang and R. Song, *Colloid Polym. Sci.*, 2014, **292**, 2949-2957.

43. J. T. Yoon, S. C. Lee and Y. G. Jeong, *Compos. Sci. Technol.*, 2010, **70**, 776-782.

44. R. M. Novais, F. Simon, P. Potschke, T. Villmow, J. A. Covas and M. C. Paiva, *J. Polym. Sci., Part A: Polym. Chem.*, 2013, **51**, 3740-3750.

45. G. X. Chen, H. S. Kim, B. H. Park and J. S. Yoon, *Macromol. Chem. Phys.*, 2007, **208**, 389-398.

46. J. T. Yoon, Y. G. Jeong, S. C. Lee and B. G. Min, *Polym. Adv. Technol.*, 2009, **20**, 631-638.

47. Y. Sun and C. B. He, *RSC Adv.*, 2013, **3**, 2219-2226.

48. H. Quan, S. J. Zhang, J. L. Qiao and L. Y. Zhang, *Polymer*, 2012, **53**, 4547-4552.

49. M. Brzezinski and T. Biela, *Mater. Lett.*, 2014, **121**, 244-250.

50. M. Brzezinski, M. Boguslawska, M. Ilcikova, J. Mosnacek and T. Biela, *Macromolecules*, 2012, **45**, 8714-8721.

51. L. P. Yang and C. Y. Pan, *Macromol. Chem. Phys.*, 2008, **209**, 783-793.

52. T. Biedron, L. Pietrzak and P. Kubisa, *J. Polym. Sci., Part A: Polym. Chem.*, 2011, **49**, 5239-5244.

53. E. Manfredi, F. Meyer, P. Verge, J. M. Raquez, J. M. Thomassin, M. Alexandre, B. Dervaux, F. Du Prez, P. Van Der Voort, C. Jerome and P. Dubois, *J. Mater. Chem.*, 2011, **21**, 16190-16196.

54. I. M. de Arenaza, J. R. Sarasua, H. Amestoy, N. Lopez-Rodriguez, E. Zuza, E. Meaurio, F. Meyer, J. I. Santos, J. M. Raquez and P. Dubois, *J. Appl. Polym. Sci.*, 2013, **130**, 4327-4337.

55. F. Meyer, J. M. Raquez, O. Coulembier, J. De Winter, P. Gerbaux and P. Dubois, *Chem. Commun.*, 2010, **46**, 5527-5529.

56. F. Meyer, J. M. Raquez, P. Verge, I. M. de Arenaza, B. Coto, P. Van Der Voort, E. Meaurio, B. Dervaux, J. R. Sarasua, F. Du Prez and P. Dubois, *Biomacromolecules*, 2011, **12**, 4086-4094.

57. Z. H. Xu, Y. H. Niu, L. Yang, W. Y. Xie, H. Li, Z. H. Gan and Z. G. Wang, *Polymer*, 2010, **51**, 730-737.

58. H. Tsuji, *Macromol. Biosci.*, 2005, **5**, 569-597.

59. X. W. Zhang, R. Nakagawa, K. H. K. Chan and M. Kotaki, *Macromolecules*, 2012, **45**, 5494-5500.

60. H. Tsuji and Y. Ikada, *Polymer*, 1999, **40**, 6699-6708.

61. P. J. Pan, J. J. Yang, G. R. Shan, Y. Z. Bao, Z. X. Weng, A. Cao, K. Yazawa and Y. Inoue, *Macromolecules*, 2012, **45**, 189-197.

62. H. W. Bai, H. L. Liu, D. Y. Bai, Q. Zhang, K. Wang, H. Deng, F. Chen and Q. Fu, *Polym. Chem.*, 2014, **5**, 5985-5993.

63. H. W. Zhao, Y. J. Bian, Y. Li, Q. L. Dong, C. Y. Han and L. S. Dong, *J. Mater. Chem. A*, 2014, **2**, 8881-8892.

64. N. Rahman, T. Kawai, G. Matsuba, K. Nishida, T. Kanaya, H. Watanabe, H. Okamoto, M. Kato, A. Usuki, M. Matsuda, K. Nakajima and N. Honma, *Macromolecules*, 2009, **42**, 4739-4745.

65. X. F. Wei, R. Y. Bao, Z. Q. Cao, W. Yang, B. H. Xie and M. B. Yang, *Macromolecules*, 2014, **47**, 1439-1448.

66. H. Yamane and K. Sasai, *Polymer*, 2003, **44**, 2569-2575.

67. H. Tsuji, H. Takai and S. K. Saha, *Polymer*, 2006, **47**, 3826-3837.

68. S. Brochu, R. E. Prudhomme, I. Barakat and R. Jerome, *Macromolecules*, 1995, **28**, 5230-5239.

69. J. Narita, M. Katagiri and H. Tsuji, *Macromol. Mater. Eng.*, 2011, **296**, 887-893.

70. S. C. Schmidt and M. A. Hillmyer, *J. Polym. Sci., Part B: Polym. Phys.*, 2001, **39**, 300-313.

71. R. Y. Bao, W. Yang, W. R. Jiang, Z. Y. Liu, B. H. Xie, M. B. Yang and Q. Fu, *Polymer*, 2012, **53**, 5449-5454.

72. Y. J. Fan, H. Nishida, Y. Shirai and T. Endo, *Polym. Degrad. Stabil.*, 2004, **84**, 143-149.

73. W. C. Huang, S. Wang, C. X. Guo, X. M. Yang, Y. W. Li and Y. F. Tu, *Polymer*, 2014, **55**, 4619-4626.

74. Z. B. Qiu and W. Guan, *RSC Adv.*, 2014, **4**, 9463-9470.

75. F. Wu, B. Zhang, W. Yang, Z. Y. Liu and M. B. Yang, *Polymer*, 2014, **55**, 5760-5772.

76. H. W. Bai, W. Y. Zhang, H. Deng, Q. Zhang and Q. A. Fu, *Macromolecules*, 2011, **44**, 1233-1237.

77. H. Tsuji and Y. Ikada, *Polymer*, 1995, **36**, 2709-2716.

*Table of Contents*

# Constructing stereocomplex structure at the interface for remarkably accelerating matrix crystallization and enhancing mechanical properties of poly(L-lactide)/multi-walled carbon nanotubes nanocomposites

Huili Liu, Dongyu Bai, Hongwei Bai*, Qin Zhang, Qiang Fu*

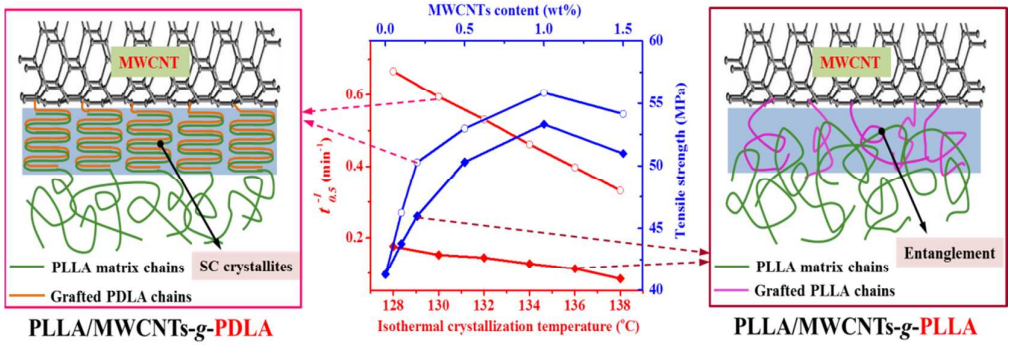


We demonstrate a facile strategy to develop high-performance PLLA/MWCNTs nanocomposites with dramatically enhanced mechanical strength and matrix crystallization rate by constructing stereocomplex structure at the interface.